Materials and Design 193 (2020) 108810

Contents lists available at ScienceDirect

Materials and Design

journal homepage: www.elsevier.com/locate/matdes

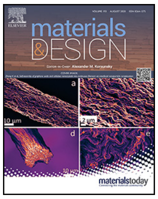

Role of infill parameters on the mechanical performance and weight reduction of PEI Ultem processed by FFF

Albert Forés-Garriga, Marco A. Pérez *, Giovanni Gómez-Gras, Guillermo Reyes-Pozo

IQS School of Engineering, Universitat Ramon Llull, Via Augusta 390, 08017 Barcelona, Spain

HIGHLIGHTS

- The role of infill parameters and printing direction on the strength and elastic properties of PEI samples is investigated.
- Experimental data allows quantifying the impact on the stiffness, resilience, maximum stress, and type of failure.
- The temperature chamber strengthens inter-layer unions improving mechanical performance and diminishes the orthotropy.
- Three-dimensional compliance matrices for six different solid and sparse configurations are provided and discussed.

GRAPHICAL ABSTRACT

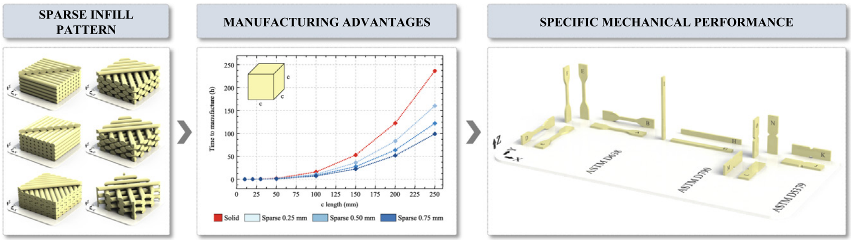

ARTICLE INFO

Article history:
Received 30 March 2020
Received in revised form 13 May 2020
Accepted 13 May 2020
Available online 20 May 2020

Keywords:
Additive manufacturing
Fused filament fabrication
PEI Ultem
Infill
Mechanical properties
Constitutive matrix

ABSTRACT

In comparison with conventional manufacturing technologies, Fused Filament Fabrication (FFF) offers countless benefits. It broadens the horizons of the design of structural components with high geometrical complexity, and lighter elements can be obtained by optimizing the infill of the part. The infill density stands as a manufacturing parameter that plays a significant part in weight reduction purposes. This fact provides FFF with an outstanding competitive advantage as compared to the rest of the additive manufacturing technologies. This work aims to investigate the role of infill parameters on the mechanical performance and weight reduction of ULTEM^{TM} 9085 samples processed by FFF, under tensile, flexural, and shear loading conditions in six different orientations with several solid and sparse configurations. Regarding the effect of the part orientation and the infill settings, the experimental results permit to draw conclusions on stiffness, resilience, maximum stress, and type of failure of the printed parts. Three-dimensional compliance matrices for each infill configuration are provided. The analysis of the results correlates the infill configuration with the mechanical performance considering the intra-layer and inter-layer unions. Finally, this research provides experimental evidence to contribute to the definition of novel design-for-manufacturing strategies for obtaining functional structural elements by FFF.

1. Introduction

A new age of digital manufacturing has transformed the way things are produced. Under the name of Industry 4.0 revolution, numerous developments are occurring at the same time in multiple fields. Additive Manufacturing (AM) is at the forefront of these transformations. In the last decade, this continually evolving technology has widened the horizons of the fabrication possibilities. This fact has led to a complete change of the way how parts are designed and produced in a wide range of sectors, including automotive, energy, aerospace, and biomedical [1]. Among the many techniques encompassed by AM [2,3], Fused Filament

---

* Corresponding author.
E-mail address: marcoantonio.perez@iqs.edu (M.A. Pérez).

https://doi.org/10.1016/j.matdes.2020.108810

Fabrication (FFF) rises above the others. This technology, also commercially known as Fused Deposition Modelling (FDM), excels mainly due to its versatility, since it is suitable for working with a wide range of materials. The evolution of FFF has positioned it as a potential candidate for the industrial sector as it allows to construct components with a high geometrical complexity that can be produced neither at low costs nor in a short time with conventional manufacturing technologies.

In this 3D printing technology, a thermoplastic filament is deposited in thin layers by an extrusion head that moves according to the building toolpaths. The material is heated a few degrees above its glass transition temperature, which causes an almost instantaneous solidification when it comes into contact with the last manufactured layer. The new layer is adhered to the adjacent one, while the volume of the whole part gets constructed. The main setting parameters are sample orientation, layer thickness, raster angle, and raster-to-raster air gap.

One remarkable feature of the FFF is its feasibility to fabricate lighter structures by optimizing the infill of the part. The infill density stands as a manufacturing parameter that plays a significant role in the strategy to reduce weight, which provides FFF with an outstanding competitive advantage as compared to the rest of AM technologies [4]. This fact, together with the development of high-performance polymeric materials with remarkable specific strength and stiffness, allows the obtention of functional structural elements. As an illustrative example, Fig. 1 depicts the role of the air gap parameter on the manufacturing time and required material volume for the production of cubes of different sizes. Data of time to manufacture in minutes and material volume in cubic centimeters is added in text boxes to notice the remarkable differences between curves when a short side length is evaluated. Each curve corresponds to a different air gap setting, as indicated in the legend.

Accordingly, the study of the mechanical performance of structures with a low infill density is of great interest to the AM community. Published contributions have been mostly focused on the mechanical analysis of the inherent anisotropy induced by the technique in solid configurations [5–7]. For instance, extensive studies of the behavior of acrylonitrile butadiene styrene (ABS) FFF parts under tensile, flexural, and compression states were conducted [8,9], as well as in fatigue conditions [10]. These results awakened the interest towards a numerical approach of the processed material [11]. Polylactic acid (PLA) was also investigated with the same purpose [12–14], and the influences of building parameters on the fatigue life were also evaluated [15]. The same analyses were attempted with polycarbonate (PC) [16], whose results provided a stiffness matrix that described the performance of this material depending on the manufacturing parameters [17]. Other investigations with the same material deepened in its fracture behavior [18,19] and the creep effect [20]. Simultaneously, other authors offered a numerical approach of its performance in fatigue conditions [21].

Among the range of thermoplastic materials analyzed in recent years, ULTEM^{TM} 9085 (PEI Ultem) [22–24] soars above the rest. This high-performance polyetherimide (PEI) offers outstanding properties for multiple industrial purposes. It features a remarkable strength-to-weight ratio and impact strength with excellent heat resistance, as well as flame-retardant capacity, and promising flame-smoke-toxicity (FST) characteristics. For all these reasons, PEI Ultem becomes especially outstanding for applications in the transport and aerospace sectors [25,26]. Thanks to applications like these, the interest in PEI Ultem keeps growing, but many areas of study are still needed to be explored. For example, its tensile behavior has been documented [27–30], as well as its response to flexural and compression tests [31–33], and its fatigue strength compared with other thermoplastics [34]. The consequences of moisture absorption in the PEI Ultem filament before printing [35] and its impact resistance [36] have also been investigated. Meanwhile, the chemical similarities between PEI Ultem and its support material pose particular challenges for the elimination of the second one. For this reason, other authors focused their work on developing a novel solvent support-removal methodology [37].

However, to the knowledge of the authors, the benefits associated with the influence of the rasters separation in terms of weight decrease, reduction of material consumption, and production time are yet not fully understood. Further, the optimization of mechanical performance by just modifying the infill configuration can be crucial to bringing this technology to the forefront of industrial manufacturing.

Accordingly, the purpose of this work is to investigate the role that the infill parameters play in the mechanical performance and weight reduction of PEI Ultem processed by FFF under multiple load conditions. This study aims to provide experimental evidence to contribute further to the definition of novel design-for-manufacturing strategies with an in-deep analysis of accurate data related to the performance of PEI Ultem. Thus, the mechanical behavior of this material is evaluated regarding the benefits of structural weight reduction, material savings, and shorter time to manufacture.

2. Methodology

2.1. Design of experiments

Tensile, flexural, and shear loading tests were conducted to identify the role that the FFF building parameters play on mechanical performance and weight reduction. The building parameters chosen for this study were sample orientation, raster angle, and raster-to-raster air gap. These parameters were used for changing the internal design of the parts. The intra-layer orientation of the filaments was set with the raster angle value. The air gap refers to the separation between two parallel rasters. Thus, the manufactured parts can be grouped into two main configurations: solid (air gap = 0 mm) and sparse (air gap > 0 mm). The design of experiments is shown in Table 1, and the manufactured part orientations are represented in Fig. 2.

In order to identify the effect of the direction of the deposited filaments on the mechanical performance of solid specimens, three

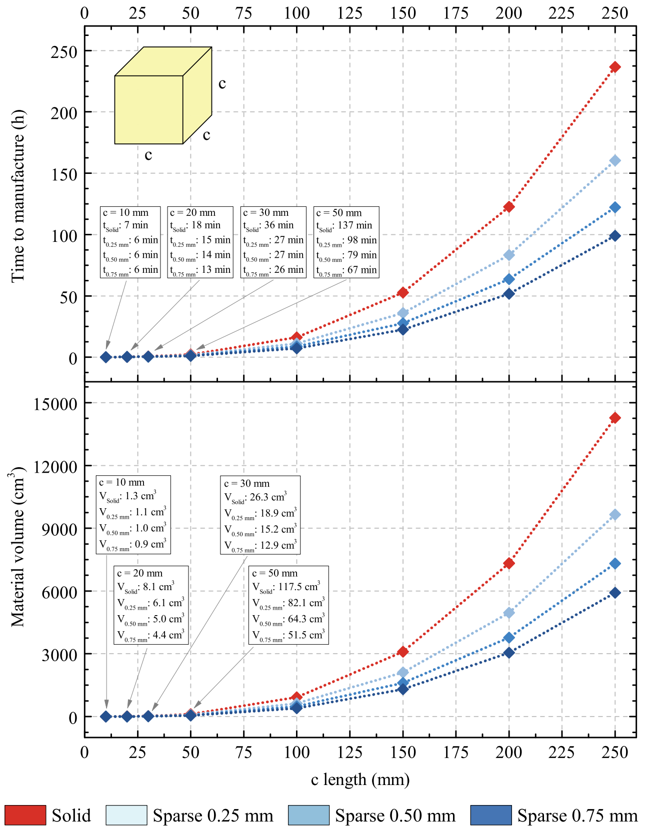

Fig. 1. Impact of the raster-to-raster air gap on the time to manufacture (top) and the material volume (bottom) of a PEI Ultem solid cube part, depending on its side length.

Table 1
Set of samples' orientations for each infill tested configuration.

ASTM test standard	Solid configuration			Sparse configuration		
	Air gap	Raster angle	Part orientation	Air gap	Raster angle	Part orientation
D638 [38]	0.00 mm	0° 90° ±45°	X-Flat/Edge Y-Flat/Edge Z-Flat/Edge	0.25 mm 0.50 mm 0.75 mm	±45°	X-Flat/Edge Z-Edge
D790 [39]	0.00 mm	0° 90° ±45°	X-Flat/Edge Z-Edge	0.25 mm 0.50 mm 0.75 mm	±45°	X-Flat/Edge Z-Edge
D5379 [40]	0.00 mm	0° 90° ±45°	X-Flat/Edge Y-Flat/Edge Z-Flat/Edge	0.25 mm 0.50 mm 0.75 mm	±45°	X-Flat/Edge Y-Flat/Edge Z-Flat/Edge

different interior raster angles were studied: 0°, 90°, and ±45°. It should be noted that not all the raster angle values may be convenient for the use of sparse for structural applications as some values may cause issues between intra-layer raster connections. Unidirectional sparse configurations dramatically reduce the consistency of these low-density parts in some particular testing directions. Therefore, only the raster angle of ±45° was considered suitable for manufacturing with any sparse configuration. Regarding the dimensions of the ASTM specimens, the considered air gap values were 0.25 mm, 0.50 mm, and 0.75 mm.

Each solid and sparse configuration was characterized in all three cartesian orientations (X, Y, and Z), as shown in Fig. 2. Due to the shape of the ASTM specimens, infill toolpaths depend on the arrangement of the part on the building bed (Flat or Edge). Thus, the possible anisotropic properties of the material have to be evaluated for every raster angle, particularly when a unidirectional configuration is used (0° or 90°).

Tensile tests were carried along the X, Y, and Z axes to verify any possible degree of isotropy in every solid configuration, and particularly the expected orthotropy in the ±45° ones. Preliminary results demonstrated that equivalent specimens were obtained if samples are rotated 90° around the Z-axis of the printing bed. Therefore, the orientations X-Flat, X-Edge, and Z-Edge were considered enough for the complete evaluation of the tensile mechanical performance of the sparse samples.

Flexural tests were conducted in all configurations to study the differences between intra-layer and inter-layer bending properties. To this end, and considering the stated equivalence of samples, specimens were manufactured and evaluated just in X-Flat, X-Edge, and Z-Edge directions for both solid and sparse configurations.

Additionally, a full factorial design of experiments was performed for the shear tests. On this account, identical part orientations were tested in both solid and sparse configurations.

To test the repeatability of all experiments, a minimum of three specimens per infill configuration were tested for each orientation, as detailed in Fig. 2. This led to a total amount of 277 tested specimens.[1]

2.2. Manufacturing of samples

A Coordinate Machine Binary file (CMB) was generated for each sample using the Insight software from Stratasys. These files include all the necessary information for manufacturing the samples according to the proposed design of experiments. The slice height value was set to 0.254 mm. All the samples were built with one external contour to accentuate the impact of the infill configuration on the mechanical performance. The seam control options were modified in order to remove the joint of the contour from the gauge section and the transition radius region. Both contour and part raster widths were established at 0.508 mm. In all cases, the minimization of the transition moves was activated, and appropriate infill trajectories were achieved by adjusting the raster angle parameter. The parallel offset part rasters feature was applied for the preparation of the solid samples that needed an infill of 0° or 90°. This avoids having a continuous defect along the height of the part when a unidirectional raster angle is selected. Different sparse configurations were generated by adding distance between filaments with the raster-to-raster air gap value.

Samples were fabricated using a Stratasys Fortus 400mc FDM equipment. This printer is equipped with a temperature chamber that ensures a controlled temperature during the entire manufacturing process. This controlled environment is crucial as it significantly enhances the inter-layer cohesion between adjacent building layers. Regarding the supplier indications, the optimum working conditions for postprocessing PEI Ultem require an oven temperature of 195°C. The extrusion temperature for the model material (PEI Ultem) is 380°C, and for the support material (PSF polysulfone) is 421°C. Once the samples were printed, support structures were removed, and the mass and the dimensions of each sample were measured before testing.

2.3. Mechanical testing

Differences in the real effective cross-sectional area and in the front surface of the tensile samples are shown in Fig. 3. The schematic 3D representations depicted in Fig. 4 show the impact that the infill configuration has on both the size and the location of the internal gaps. However, for the sake of simplicity, the nominal section measurements were used for the stress calculations.

2.3.1. Experimental setup

Tensile, flexural, and shear tests were performed using ZwickRoell Z030 equipment. A 3D Digital Image Correlation (DIC) setup was integrated for the investigation of full-field deformation in tensile and shear tests. Two Allied Vision GigE MAKO G-507B cameras with APO-Xenoplan 1.4/23–0903 lens were used for recording the displacements on the surface of the samples. Specimens were previously sprayed with a black and white stochastic pattern. The system was calibrated with a GOM Correlate CP20/MV55x44 panel. The video sequences were treated with GOM Correlate Professional software to analyze the full-field deformation of the samples.

2.3.2. Tensile testing

Tensile tests were conducted following the ASTM D638 standard [38] (see Fig. 2). Specimen type IV was chosen with a thickness of 4 mm. The yield point was determined with an offset method of 0.1% strain. Two perpendicular DIC extensometers placed in the center of the gauge section of each specimen were used for the calculation of the Poisson's coefficients within the elastic region. Results of tensile modulus, yield stress, yield strain, tensile strength, and strain at tensile strength were reported.

2.3.3. Flexural testing

Three-point bending tests were conducted following the ASTM D790 standard [39] (see Fig. 2). The thickness of the specimens was set to 4 mm. The geometry of samples was defined with 64 mm support span, 10 mm width, and 127 mm length, in agreement with the test

---

[1] Tensile testing: 115 samples (70 solid and 45 sparse). Flexural testing: 54 samples (27 solid and 27 sparse). Shear testing: 108 samples (54 solid and 54 sparse).

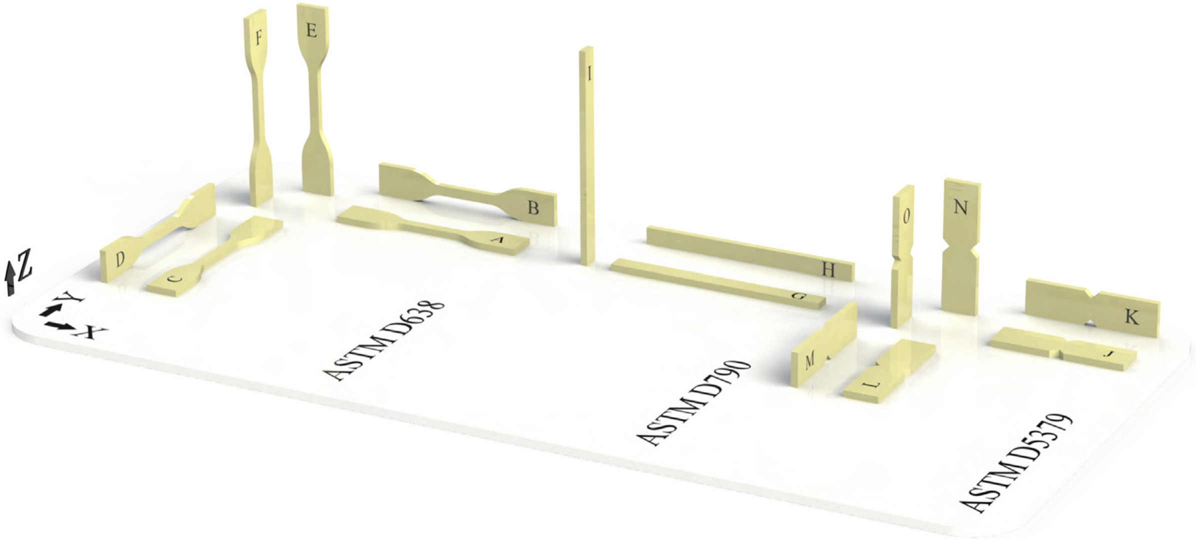

Fig. 2. Building orientations of all the manufactured test samples. ASTM D638 [38]: X-Flat (A), X-Edge (B), Y-Flat (C), Y-Edge (D), Z-Flat (E), Z-Edge (F); ASTM D790 [39]: X-Flat (G), X-Edge (H), Z-Edge (I); ASTM D5379 [40]: X-Flat (J), X-Edge (K), Y-Flat (L), Y-Edge (M), Z-Flat (N), Z-Edge (O).

standard. Under these conditions, the rate of crosshead displacement resulted in 1.71 mm/min. The yield point was determined with an offset method of 0.1% strain. Although ASTM D790 suggests ending the test when a 5% of strain is reached, all the samples were tested until failure occurred. Flexural modulus, yield stress, yield strain, flexural strength, and strain at flexural strength results were reported.

2.3.4. Shear testing

ASTM D5379 test standard [40] (see Figs. 2 and 5) was followed for shear testing. The thickness of the specimens was set to 4 mm. With the used samples, no twisting effect was observed during the test. Therefore, the use of additional tabs was unnecessary. DIC equipment allowed the measurement of the shear strain at the center of the specimen. Although the test standard recommends stopping the test when a 5% of strain is reached, the shear tests were conducted until failure occurred. The yield point was estimated using the offset method with a strain of 0.2%. Shear modulus, yield point data, shear strength, and strain at shear strength values were reported.

3. Results and discussion

3.1. Tensile testing

Fig. 6 shows representative data from the tensile tests conducted with the configurations previously described (see Fig. 2). Apparent differences in stress and strain values can be observed between samples. However, some samples present brittle fracture while others show a larger plastic region. It should be noted that, in the case of sparse configurations, the stress axis has been scaled for the reader's convenience.

Fig. 7 shows the results of tensile testing. The charts in the left column collect the results of the following tensile properties: tensile modulus, yield stress, strain at yield stress, and maximum stress and its corresponding strain. On the one hand, it was observed that the toolpaths in the gauge region have minor differences if the arrangement is Flat (6 × 4 mm) or Edge (4 × 6 mm). Thus, the mean value and the corresponding standard deviation of the results were calculated for every test orientation (X, Y, and Z) regardless of the fabrication arrangement (Flat or Edge). On the other hand, the charts in the right side of the figure show mass-normalized values of the properties mentioned above. These average values have been calculated by dividing the obtained test results of each specimen over its corresponding mass.

Focusing on the left column graphs, all solid configurations achieve similar results regardless of the orientation of the rasters, especially in the elastic region (charts *a*, *c*, and *e*). These results indicate the existence of an orthotropic behavior that does not become as outstanding as it was initially expected. This fact can be attributed to the strength of the existent joints between coplanar filaments (intra-layer unions) and between adjacent layers (inter-layer unions). The used 3D printer ensures that the temperature in the building chamber is tightly controlled during the entire manufacturing process to enhance this phenomenon. This reduces the thermal shock that takes place when the extruded filament is deposited and enters in contact with the last built layer to improve the quality of the final parts.

Nonetheless, the maximum strength of the specimens in the Z test orientation is markedly inferior to that achieved in the X and Y directions (51.2, 44.3% of reduction for 0°; 39.0, 44.7% for 90°; and 36.8, 39.1% for ±45° in X, Y directions, respectively). Furthermore, specimens oriented along the X or Y axes show a plastic fracture caused by the elongation of the deposited filaments. The fracture in the Z direction tests leads to the separation of two contiguous layers in manufacturing, which happens abruptly, resulting in a brittle type of failure. Thus, obtained results state the lower resistance of the joints between layers in comparison to that of the filament itself. This fact confirms a remarkable degree of orthotropy when the strength of the processed material is evaluated.

The results also verify that a 90° rotation of the parts around the Z-axis when manufacturing has insignificant effects on the mechanical properties. This equivalence of samples could initially be expected by analyzing the toolpaths generated in the CMB file. Furthermore, the noticeable similarities while comparing the experimental results obtained in the $X_{0^{\circ}}$-$Y_{90^{\circ}}$, $X_{90^{\circ}}$-$Y_{0^{\circ}}$, and $X_{\pm 45^{\circ}}$-$Y_{\pm 45^{\circ}}$ configurations evidence this hypothesis. These results confirm the reproducibility of the professional printer for manufacturing parts with the same toolpaths regardless of their rotation around the Z-axis on the building bed. The application of this assumption of equivalence of samples made it possible to remove the Y orientations from the design of experiments of the tests to perform with the sparse configurations.

Tests on sparse samples conclude that similar results are seen in the X orientation regardless of the degree of densification used. However, this air gap parameter appears to have a more evident impact when the material is evaluated in the Z orientation. This

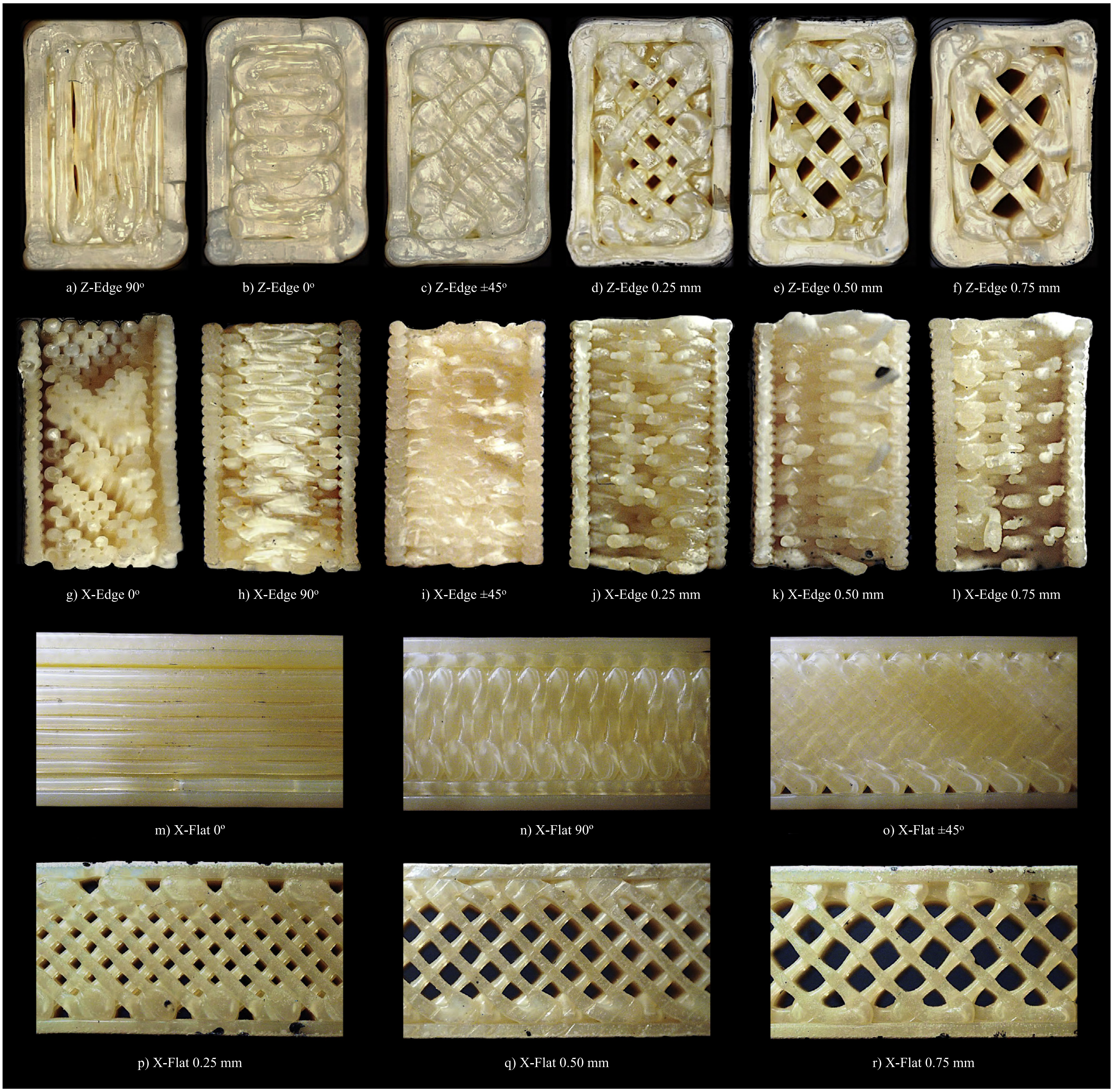

Fig. 3. Effective cross-sectional area (6 mm × 4 mm) (sub-figures a-l) and front surface (sub-figures m-r) of tensile samples in solid and sparse configurations (see Table 1).

observation can be explained by the significant reduction in the resistant cross-section with the modification of the air gap design parameter, which directly affects the mechanical performance of the specimens. The effect is minor in Flat samples because the effective cross-section is perpendicular to the building direction of the sparse structure (see Figs. 3 and 4).

Nevertheless, the results of the specific mechanical properties (charts in the right column) demonstrate a much more evident effect of the use of the sparse configurations. When the mass of the specimens is taken into account, the reduction of material in the effective cross-section of the sample is somehow quantified. On some occasions, sparse configurations show similar or even better specific mechanical properties to those of the equivalent $\pm 45^{\circ}$ solid family (commonly predefined for manufacturing). This fact can be seen in the specific deformation values achieved in the elastic and plastic zones.

3.2. Flexural testing

Fig. 8 depicts representative curves of solid (top) and sparse (bottom) configurations from the flexural tests. As before, the stress-strain curves differ in stiffness, maximum load, and material failure depending on the internal construction of the samples and the direction of testing. The shaded area of the graphs corresponds to the 5% strain threshold indicated in the ASTM D790 standard [39]. The nomenclature used on the labels refers to the manufacturing orientations detailed in Fig. 2.

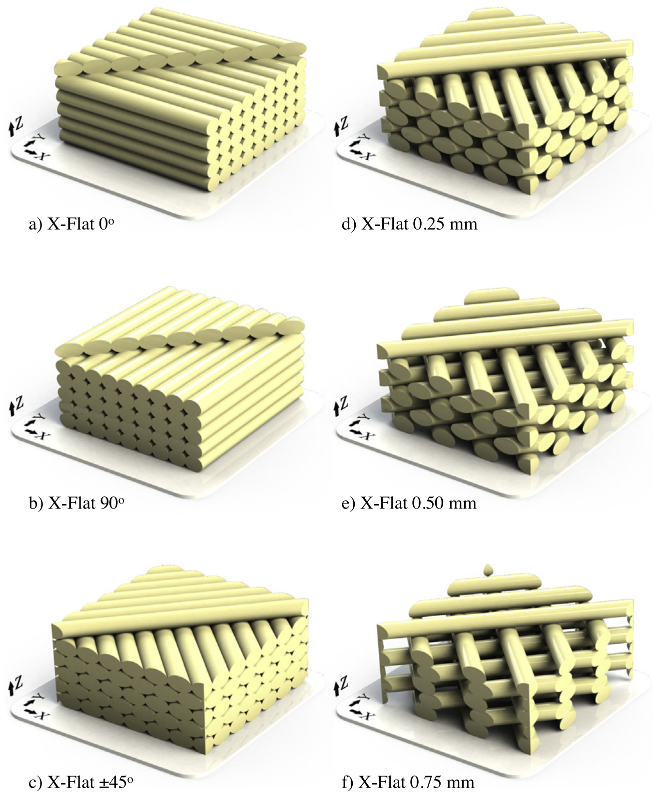

a) X-Flat 0º
d) X-Flat 0.25 mm
b) X-Flat 90º
e) X-Flat 0.50 mm
c) X-Flat ±45º
f) X-Flat 0.75 mm

Fig. 4. Representation of the cross-sectional area of samples in X-Flat 0° (a), X-Flat 90° (b), and X-Flat ±45° (c) solid configurations, and X-Flat 0.25 mm (d), X-Flat 0.50 mm (e), and X-Flat 0.75 mm (f) sparse configurations (see Table 1).

Fig. 9 shows the results of the following flexural properties (charts in the left column): flexural modulus, yield stress, strain at yield stress, and maximum stress and its corresponding strain. In graphs *e* and *i*, the 5% of strain threshold is indicated. Applying again the assumption of equivalence of samples stated in tensile tests, the results from flexural tests were determined for X-Flat, X-Edge, and Z-Edge orientations exclusively. The charts shown in the right column of the figure correspond to the equivalent specific values of each of the properties to ease data interpretation. These values were calculated by normalizing according to the mass of each sample.

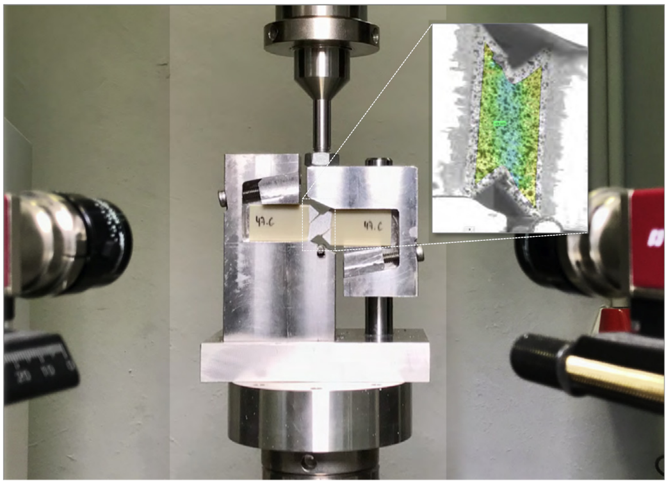

Fig. 5. Experimental setup for ASTM D5379 shear test standard with Digital Image Correlation equipment.

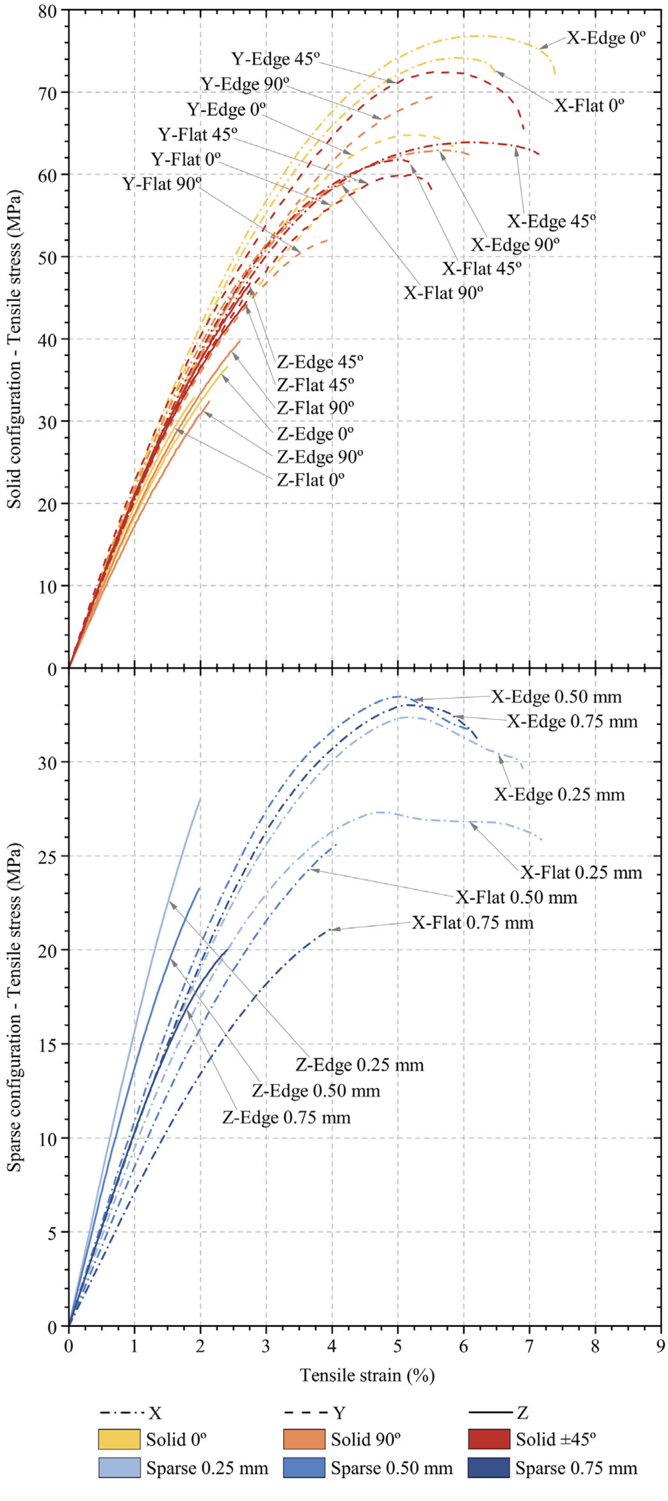

Fig. 6. Representative stress-strain data from the tensile test results of solid (top) and sparse (bottom) configurations with the different orientations of rasters and infill densities (see Fig. 2).

When flexural test results are compared with the data from the tensile tests, an inferior degree of isotropy is observed when the load is below the elastic limit. Minor differences are observed on the flexural moduli (X-Flat, X-Edge, and Z-Edge) of all solid samples (2260, 2360, 1950 MPa for 0°; 1847, 2112, 2073 MPa for 90°; and 1942, 2299, 1979 MPa for ±45°). However, noticeable deviations appear between

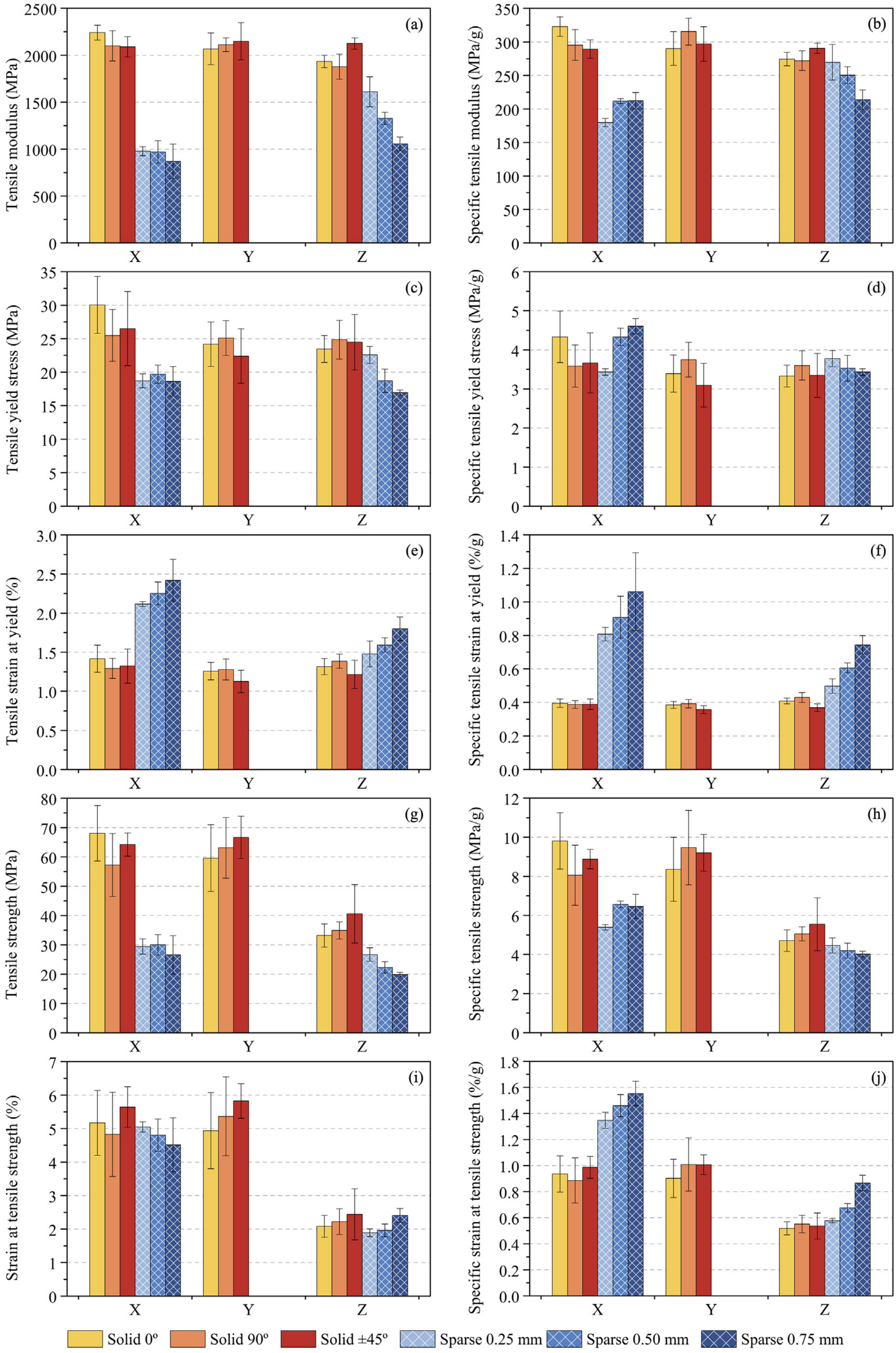

Fig. 7. Tensile test results comparision between solid and sparse configurations: tensile modulus (a), specific tensile modulus (b), tensile yield stress (c), specific tensile yield stress (d), tensile strain at yield (e), specific tensile strain at yield (f), tensile strength (g), specific tensile strength (h), strain at tensile strength (i), and specific strain at tensile strength (j).

the X-Flat and X-Edge test orientations when the yield point (charts *c* and *e*) and the maximum load (charts *g* and *i*) are analyzed. The highest and lowest values for stress and strain can be observed for 0° and 90° configurations, respectively. This occurs because the 90° configuration samples have intra-layer filaments parallel to the stress plane. In contrast, the 0° configuration specimens have the infill rasters perpendicular to the

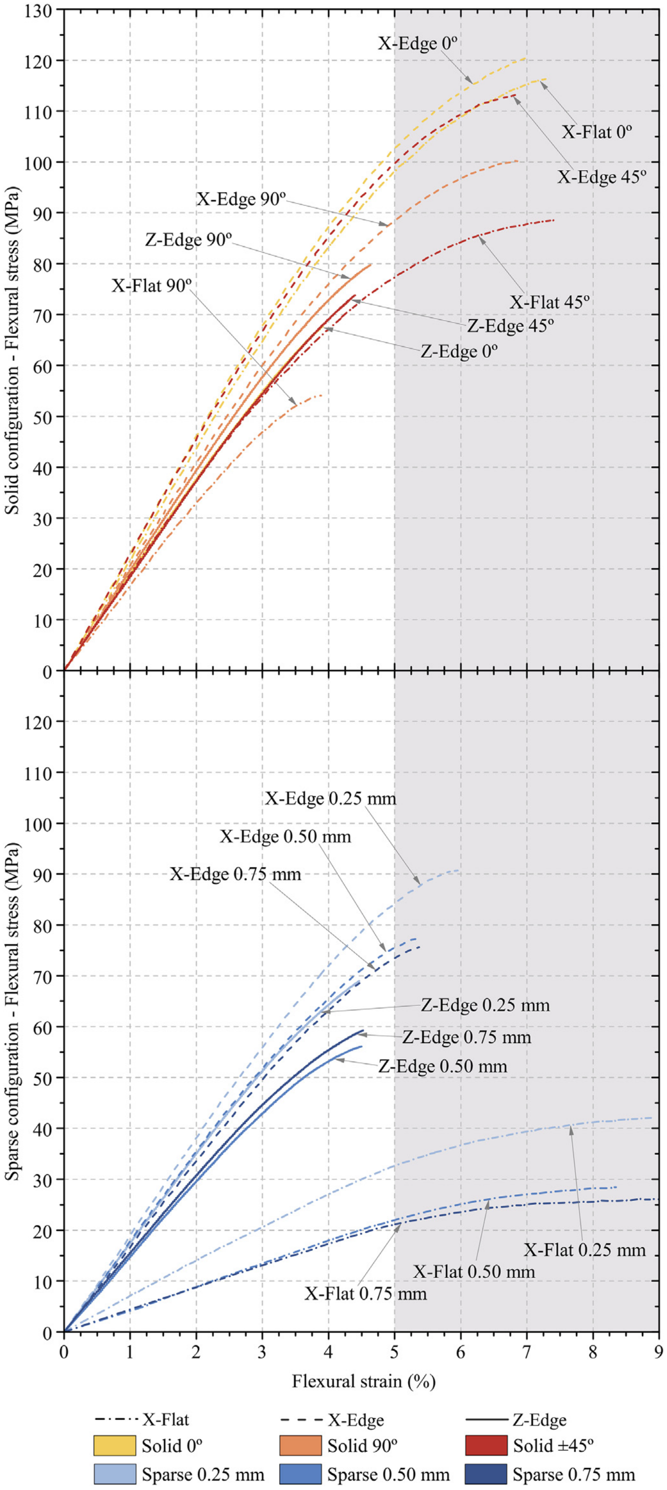

Fig. 8. Representative stress-strain data from the flexural test results of solid (top) and sparse (bottom) configurations with the different orientations of rasters and infill densities stated in Fig. 2. The beginning of the shaded area, where the major part of breaks occurs, refers to the calculation threshold established in the ASTM D790 [39] standard.

stress plane. Hence, the results indicate that both the resilience and the bending tenacity of solid samples are lower when the intra-layer unions support the stress. As an example, charts *c* and *e* in Fig. 9 show that the resilience of the samples is lower when the raster angle is set to 90°, and it increases when this parameter is set to ±45°. The maximum resilience is achieved when the orientation of the filaments coincides with the direction of the tensioned fiber (raster angle of 0°).

The sparse infill configuration shows a markedly different behavior between the X-Flat samples, and the X-Edge and Z-Edge specimens. Although the nominal second moment of inertia ($I = \frac{b \times h^3}{12}$) of all sections is equivalent,[2] the effective cross-sections are significantly different (see Figs. 3 and 4) depending on the testing orientation. Moreover, the layer contours in the outside of the specimen act as a reinforcement skin in the direction of the outer fiber in both X-Edge and Z-Edge orientations. Nevertheless, the X-Flat samples do not have any skin on the outer tensioned layer, so their stiffness is directly equivalent to that of the sparse core. This observation explains the noticeable differences between the values presented in chart *a* of Fig. 9.

When comparing mass-normalized values, the sparse configurations X-Edge and Z-Edge directions resemble average values achieved by the solid typologies. But the main variations occur in the X-Flat orientation. In this case, the specific mechanical performance of the sparse samples is notably close to the results stated by the solid ones, particularly for the yield point and peak strength values. Additionally, their specific deformation values at these points are above those of the solid families, and there is a three-fold increase in the X-Flat direction samples in particular.

These results prove that sparse configurations can be a suitable substitute for solid parts. However, the advantages become more apparent when they are used in geometries with large surfaces parallel to the printing bed. In those situations, the introduction of an air gap between the rasters decreases the mass and the cost of the parts significantly while maintaining similar mechanical properties overall.

3.3. Shear testing

Fig. 10 depicts the selected data from the results of the shear tests performed in solid (top) and sparse (bottom) configurations. The stress-strain curves differ in stiffness, maximum load, and material failure depending on the infill configuration and the direction of testing. In the case of sparse configurations, as before, the stress axis has been scaled for the reader's convenience. The shaded area of the graphs resembles the 5% strain threshold indicated in the ASTM D5379 standard [40], corresponding to 50 mε. The nomenclature used on the labels refers to the manufacturing orientation displayed in Fig. 2.

Fig. 11 displays the following shear properties (charts in the left column): shear modulus, yield stress, strain at yield stress, and maximum stress, as well as its corresponding strain. In charts *e* and *i*, the 50 mε of strain threshold is indicated. The charts on the right side of the figure show the mass-normalized values of the properties mentioned above, considering the mass of each tested sample.

Depicted results are average values obtained by testing the two possible arrangements of samples belonging to the same plane. As displayed in Fig. 2, the X-Flat (J) and Y-Flat (L) samples are contained in the same XY plane, but they have their infill filaments arranged in different alignments. The same applies to the X-Edge (K) and Z-Flat (N) samples in the XZ plane, and the Y-Edge (M) and Z-Edge (O) in the YZ plane. The obtained data shows that there is a distinct behavior between the samples contained in the same plane (Fig. 11). These differences are attributed to the modification of the effective cross-section of samples, due to the arrangement of filaments and layers. Accordingly, an average value was determined for each orthogonal plane (XY, XZ, and YZ) to calculate the constitutive matrix.

As shown in Fig. 11, the results for X-Flat and Y-Flat (XY and YX arrangements) with an air gap of 0.75 mm could not be determined. Due to the limited amount of rasters in this particular infill configuration, no recognizable stochastic pattern could be obtained for an accurate enough DIC post-process. Therefore, the mechanical properties results are only presented for the rest of the arrangements of this sparse

---

[2] 0.25 mm air gap samples averaged an inertia of 64.11 mm^4, while 64.51 mm^4 was registered by the 0.50 mm specimens, and 64.32 mm^4 by the 0.75 mm ones.

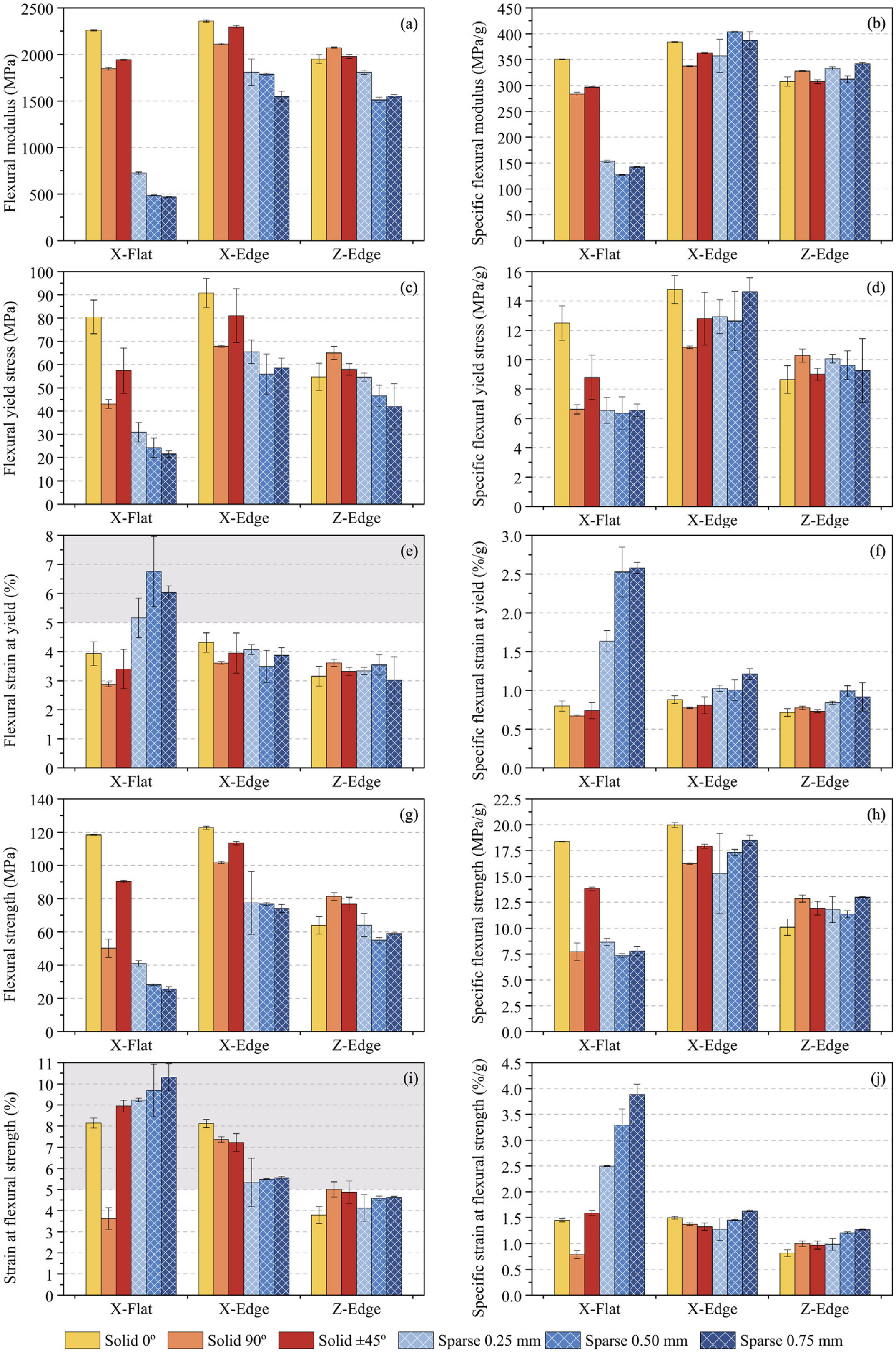

Fig. 9. Flexural test results comparision between solid and sparse configurations: flexural modulus (a), specific flexural modulus (b), flexural yield stress (c), specific flexural yield stress (d), flexural strain at yield (e), specific flexural strain at yield (f), flexural strength (g), specific flexural strength (h), strain at flexural strength (i), and specific strain at flexural strength (j).

typology. Additionally, the yield point of the X-Flat (XY) orientation with a 0.50 mm air gap could not be determined using the offset method indicated above.

Focusing on the charts in the left column of Fig. 11, solid and sparse configurations have different trends in the six evaluated arrangements. The equivalency of samples assumed from solid tensile test results is

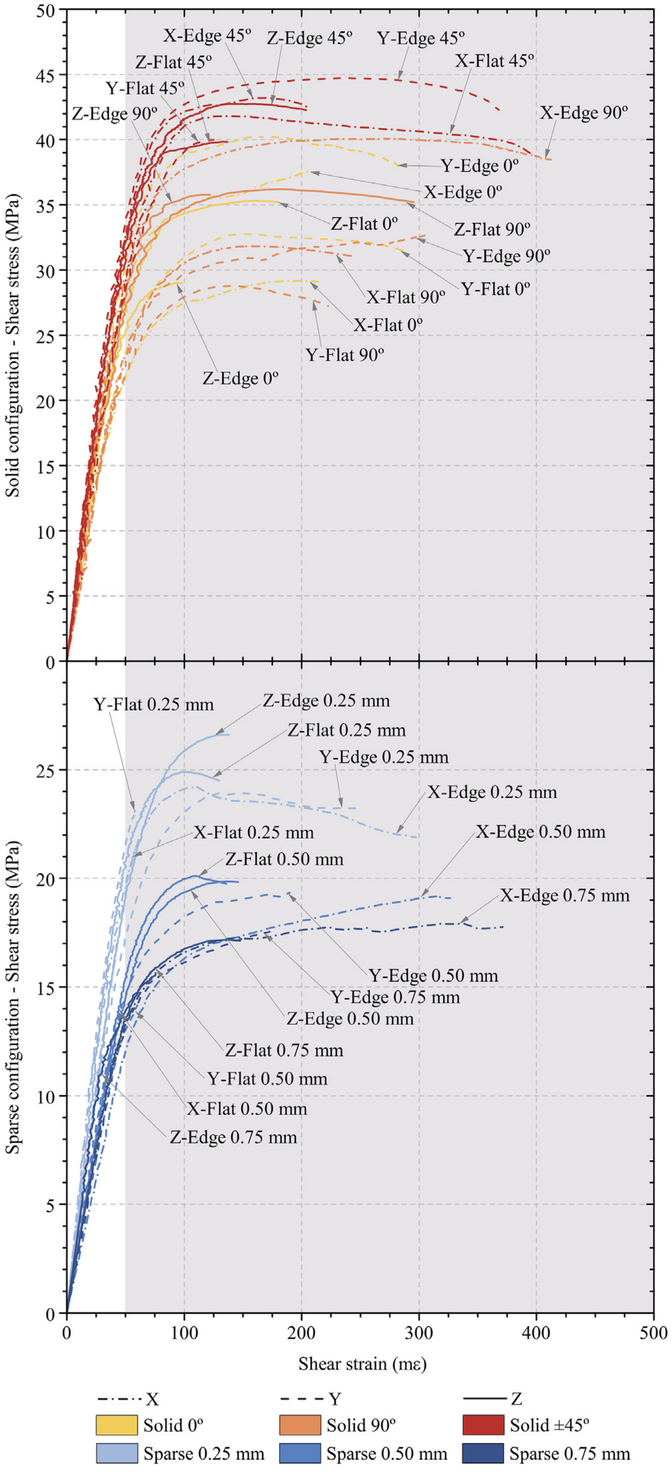

Fig. 10. Representative stress-strain data from the shear test results of solid (top) and sparse (bottom) configurations with the different orientations of rasters and infill densities stated in Fig. 2. The beginning of the shaded area, where the major part of breaks occurs, refers to the calculation threshold established in the ASTM D5379 [40] standard.

still noticeable. Actually, XY and YX results should be treated together, as well as the XZ and YZ, and the ZX and ZY. Furthermore, the raster orientation in the solid unidirectional configurations (0° and 90°) must be taken into account. Thus, the XY results of the 0° solid family are equivalent to the 90° results of the YX arrangement and vice versa. Similarly, the same deduction can be applied to the results of XZ and YZ dispositions, and those of ZX and ZY.

The analysis of the results of shear modulus from the solid samples concludes that very close values of stiffness are obtained with the 0° and 90° configurations. In all tests, the ±45° infill configuration presents superior rigidity. Regarding the sparse typologies, all samples display slightly higher values in the XY and YX arrangements (427, 477 MPa for 0.25 mm; and 328, 293 MPa for 0.50 mm in XY and YX arrangements, respectively). Moreover, the results prove the hypothesis that an increment of the air gap value leads to a decrease in stiffness, as expected.

As can be seen, yield stress values for the solid configurations are similar, being the ±45° samples the ones that offer higher results as compared to the 0° and 90° configurations. In the case of the sparse samples, the stress values obtained in the vertical arrangements (ZX and ZY) reduce significantly as the air gap value increases. Particularly, the obtained mean stresses at yield for solid ±45° samples were 29.3 MPa in ZX and 27.1 MPa in ZY. When a positive air gap is used, these values decrease to 18.9 MPa and 18.6 MPa for 0.25 mm, 15.6 MPa, and 16.1 MPa for 0.50 mm, and 13.7 MPa and 13.7 MPa for 0.75 mm, respectively. In samples manufactured in XZ and YZ, the increase in the air gap appears not to compromise this property.

At this point, it should be noted that the DIC post-process of shear test requires that a larger area of the pattern must be recognized during all the tests as a GOM Surface Component needs to be created. This fact results in a reduction of the DIC post-process accuracy in the shear tests in comparison with the tensile ones, which demand a 2-point extensometer. Thus, the wider dispersion of the results from shear tests makes it more challenging to find notable changes in this property. Nevertheless, as stated above, some trends can be observed that fit the hypothesis of this paper.

In contrast, the maximum strength values of the solid specimens show some clear tendencies. The sample equivalence already observed with the results from the tensile tests becomes even more evident. Specimens from 0° solid configuration exhibit lower strength in the XY and XZ directions. As the infill filaments are deposited perpendicularly to the resistant cross-section, they shear and slide during the test until the intra-layer unions (XY) or the inter-layer ones (XZ) fail. In vertical samples, the superior strength of this solid configuration is reached when the number of intra-layer filament unions in the effective cross-section is higher (ZY direction). In 90° solid configuration, the same phenomenon is observed in the YX, YZ directions, and, to a minor extent, in the ZX. This effect is not seen in the ±45° solid configuration, which has similar strength values in all arrangements. Also, this phenomenon is not appreciated in the sparse typologies. In these cases, the maximum strength decreases as the air gap increases.

Finally, the trends are slightly different when considering the normalized value of every property (charts in the right column). The specific stiffness results from XY and YX sparse samples are comparable to the ones from their solid counterparts. Moreover, the values from the sparse XZ, YZ, ZX, and ZY arrangements are also analogous to those of the solid ones. The same result can be found between sparse and solid configurations regarding yield stress properties. However, considering the deviations of the obtained results, their specific strains at this point are significantly higher as compared to those when no air gap is used. Furthermore, the mass contribution also sets the specific strength values of the sparse configurations slightly below those obtained by the solid families.

3.4. Compliance matrices

Table 2 (solid) and Table 3 (sparse) collect the average values and their corresponding standard deviation of the measured engineering constants. Analogous data already published from equivalent infill configurations is presented for comparison. As stated before, in some tests the thickness of the samples or the limited amount of rasters of some infill configurations compromised the accuracy of the DIC post-process. Accordingly, no data is presented for those cases when the stochastic pattern was not correctly recognized.

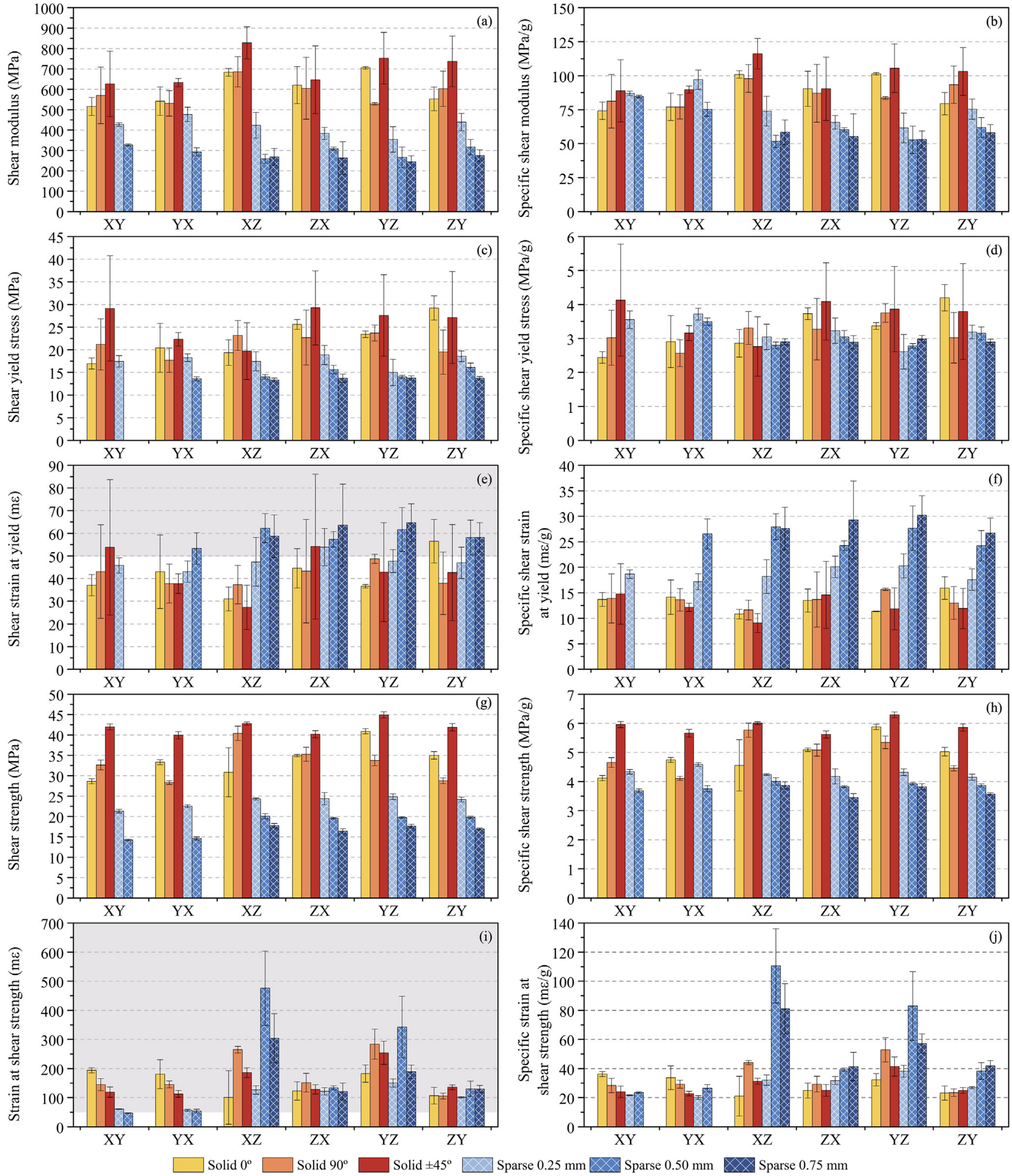

Fig. 11. Shear test results comparision between solid and sparse configurations: shear modulus (a), specific shear modulus (b), shear yield stress (c), specific shear yield stress (d), shear strain at yield (e), specific shear strain at yield (f), shear strength (g), specific shear strength (h), strain at shear strength (i), and specific strain at shear strength (j).

Based on the experimental results, the compliance matrix S for each studied configuration was calculated. Fig. 12 depicts the obtained compliance matrices describing the orthotropic elastic behavior of PEI Ultem parts processed by FFF in every one of the solid and sparse configurations investigated. The components of the diagonal correspond to: $S_{11}=\frac{1}{E_X}$, $S_{22}=\frac{1}{E_Y}$, $S_{33}=\frac{1}{E_Z}$, $S_{44}=\frac{1}{G_{YZ}}$, $S_{55}=\frac{1}{G_{XZ}}$, and $S_{66}=\frac{1}{G_{XY}}$; while the extension-extension coupling elements were calculated as: $S_{12}=mean(-\frac{\nu_{YX}}{E_Y},-\frac{\nu_{XY}}{E_X})$, $S_{13}=mean(-\frac{\nu_{ZX}}{E_Z},-\frac{\nu_{XZ}}{E_X})$, and $S_{23}=mean(-\frac{\nu_{ZY}}{E_Z},-\frac{\nu_{YZ}}{E_Y})$. The extension-shear and shear-shear coupling elements are zero due to the orthotropic assumption.

Table 2
Comparison of the obtained engineering constants of the PEI Ultem with those published in the literature for solid configurations.

Raster angle	Tensile moduli (MPa)			Flexural moduli (MPa)			Shear moduli (MPa)			Poisson's ratio					
	E_X	E_Y	E_Z	E_{X-Flat}	E_{X-Edge}	E_{Z-Edge}	G_{XY}	G_{XZ}	G_{YZ}	ν_{XY}	ν_{YX}	ν_{XZ}	ν_{ZX}	ν_{YZ}	ν_{ZY}
0°	2242 ±79	2069 ±168	1935 ±67	2260 ±7	2360 ±10	1950 ±49	529 ±41	652 ±47	629 ±29	0.351 ±0.037	N/A	0.367 ±0.042	0.297 ±0.008	N/A	N/A
90°	2100 ±160	2113 ±74	1879 ±133	1847 ±16	2112 ±10	2073 ±7	551 ±76	646 ±84	566 ±44	0.328 ±0.047	N/A	0.387 ±0.053	0.389 ±0.083	0.352 ±0.029	N/A
±45°	2092 ±108	2150 ±198	2126 ±61	1942 ±3	2299 ±13	1979 ±22	630 ±81	737 ±92	745 ±89	0.344 ±0.007	N/A	0.392 ±0.002	0.348 ±0.029	N/A	N/A
±45°[a]	–	2510 ±60	2410 ±15	–	2400 ±30	2120 ±80	–	–	–	–	–	–	–	–	–
±45°[b]	2245 ±124	2280 ±385	2030 ±199	–	–	–	–	–	–	0.370	0.370	0.390	0.330	–	–
±45°[c]	1747 ±102	–	2092 ±130	–	–	–	–	–	–	–	–	–	–	–	–
±45°[d]	–	–	–	- 1875 ±12	2384 ±16	–	–	–	–	–	–	–	–	–	–
0°[e]	–	–	–	2233	–	–	–	–	–	–	–	–	–	–	–
90°[f]	–	–	–	2109	–	–	–	–	–	–	–	–	–	–	–
0°[g]	–	–	–	2351	–	–	–	–	–	–	–	–	–	–	–
90°[h]	–	–	–	1992	–	–	–	–	–	–	–	–	–	–	–
±45°[i]	1930 ±20	2090 ±30	–	–	–	–	–	–	–	–	–	–	–	–	–

[a] [22,23] Air gap 0.00 mm; Number of contours: 1; Contour width: N/A; Raster width: N/A.
[b] [27] Air gap 0.00 mm; Number of contours: N/A; Contour width: N/A; Raster width: N/A.
[c] [29] Air gap 0.00 mm; Number of contours: 1; Contour width: 0.508 mm; Raster width: 0.508 mm.
[d] [31] Air gap 0.00 mm; Number of contours: 1; Contour width: 0.508 mm; Raster width: 0.508 mm.
[e] [33] Air gap −0.0254 mm; Number of contours: 1; Contour width: 0.4064 mm; Raster width: 0.4064 mm.
[f] [33] Air gap −0.0254 mm; Number of contours: 1; Contour width: 0.4064 mm; Raster width: 0.4064 mm.
[g] [33] Air gap 0.00 mm; Number of contours: 1; Contour width: 0.4064 mm; Raster width: 0.4064 mm.
[h] [33] Air gap 0.00 mm; Number of contours: 1; Contour width: 0.4064 mm; Raster width: 0.4064 mm.
[i] [35] Air gap 0.00 mm; Number of contours: N/A; Contour width: N/A mm; Raster width: N/A mm.

Table 3
Comparison of the obtained engineering constants of the PEI Ultem with those published in the literature for sparse configurations.

Air gap (mm)	Tensile moduli (MPa)			Flexural moduli (MPa)			Shear moduli (MPa)			Poisson's ratio					
	E_X	E_Y	E_Z	E_{X-Flat}	E_{X-Edge}	E_{Z-Edge}	G_{XY}	G_{XZ}	G_{YZ}	ν_{XY}	ν_{YX}	ν_{XZ}	ν_{ZX}	ν_{YZ}	ν_{ZY}
0.25	978 ±48	N/A	1612 ±159	726 ±11	1809 ±143	1809 ±22	452 ±18	403 ±35	397 ±38	0.436 ±0.024	N/A	0.289 ±0.044	N/A	N/A	0.281 ±0.056
0.50	969 ±119	N/A	1329 ±65	487 ±4	1788 ±12	1512 ±30	310 ±10	284 ±12	291 ±31	0.546 ±0.085	N/A	0.388 ±0.087	N/A	N/A	0.276 ±0.023
0.75	870 ±183	N/A	1056 ±73	468 ±4	1548 ±57	1554 ±16	N/A	266 ±45	260 ±20	0.505 ±0.071	N/A	0.363 ±0.017	N/A	N/A	0.241 ±0.076
2.54[a]	–	–	–	- 1786 ±26	1847 ±43	–	–	–	–	–	–	–	–	–	–

[a] [31] Raster angle ±45°; Number of contours: 1; Contour width: 0.508 mm; Raster width: 0.508 mm.

The extension coefficients[3] of the matrices of solid configurations confirm a similarity between the X and the Y axes (i.e., $S_{11} = S_{22}$) regardless of the orientation of the infill rasters. Slightly higher flexibility is observed in Z-direction in 0° and 90° samples (i.e., $S_{33} > S_{11}$), as expected. The $\pm 45^{\circ}$ configuration holds an equivalent Z-performance to X and Y results (i.e., $S_{33} \approx S_{11} \approx S_{22}$). This experimental observation may be considered to be related to the intra-layer and inter-layer cohesion. During the deposition of the material, the difference in temperature between contiguous filaments (intra-layer) is significantly lower than the thermal gradient between adjacent layers (inter-layer). As a result, the bond between parallel filaments is more rigid and resistant than the one between layers. Specifically, the oven temperature was set at 195°C, while the PEI Ultem extrusion temperature was 380°C. This evidence may explain why the stiffness in the filament direction is higher than between filaments.

Regarding the shear components, in all three solid configurations, higher flexibility is identified in the XY-plane (i.e., S_{66}). In contrast, despite some unavailable Poisson's ratio results, the impact of the direction of the infill rasters on the extension-extension coupling coefficients[4] appears to be negligible (i.e., $S_{12} \approx S_{13} \approx S_{23}$). Furthermore, if the flexibility of these configurations is analyzed, the $\pm 45^{\circ}$ raster angle provides a stiffer intra-layer and inter-layer cohesion than any unidirectional configuration.

Some authors [41,42] have recently assumed that, under a plane stress state, the printed parts present a transversely isotropic behavior of the plane parallel to the building bed. This hypothesis can be examined here from matrices presented in Fig. 12. Thus, an isotropic transverse behavior of the XY plane on a general stress state would be reflected as $S_{11} = S_{22}$, $S_{13} = S_{23}$, $S_{44} = S_{55}$, and the component $S_{66}^{Iso} = \frac{1}{G_{XY}} = \frac{2(1+\nu_{XY})}{E_X} = 2(S_{11} - S_{12})$. However, not all these component conditions are satisfied in this general stress state. Major differences are found on components S_{66}. For example, in the 0° solid configuration $S_{66}^{Iso} = 1.205\ GPa^{-1} < S_{66}^{Exp} = 1.891\ GPa^{-1}$. Analogous analyses could be done for the 90°[5] and ±45°[6] configurations considering the same plane. Another approach would be to assume a transversely isotropic behavior of the plane perpendicular to the filaments. Accordingly, in the 0° solid configuration, an isotropic transverse behavior of the YZ plane would be reflected as $S_{22} = S_{33}$, $S_{12} = S_{13}$, $S_{55} = S_{66}$ and the component $S_{44}^{Iso} = \frac{1}{G_{YZ}} = \frac{2(1+\nu_{YZ})}{E_Y} \approx 1.294\ GPa^{-1}$. Analogous analyses could be done for the 90° configuration regarding the XZ plane, and for the ±45° configuration considering both YZ and XZ planes. As before, the component conditions are not satisfied.

Overall, the experimental results show a more flexible behavior in the shearing plane than the transverse isotropy hypotheses. Consequently, the results of this investigation do not recognize transversely isotropic behavior neither on the plane XY, nor on the plane perpendicular to the filaments.

In the right column of Fig. 12, the results of the matrices of the sparse configurations are given. It should be noted that S_{22} components have taken the value of S_{11} since the corresponding tests were not conducted, following the conclusions drawn from the tensile tests with solid samples. As can be seen, the sparse compliance matrices display higher values than the solid ones, as expected. This fact agrees with the increased flexibility of the printed parts due to the addition of the air gap between filaments. Besides that, stiffness is less compromised in sparse configurations on Z-direction, as demonstrated by the fact that

---

[3] Extension coefficients were determined considering the tensile moduli results.

[4] Extension-extension coupling coefficients were determined considering the tensile moduli results.

[5] $S_{66}^{Iso} = 1.265\ GPa^{-1} < S_{66}^{Exp} = 1.816\ GPa^{-1}$.

[6] $S_{66}^{Iso} = 1.285\ GPa^{-1} < S_{66}^{Exp} = 1.587\ GPa^{-1}$.

Compliance matrix S in GPa^{-1}
for solid 0° configuration

$$\begin{bmatrix} \underset{\pm 0.016}{0.446} & \underset{\pm 0.018}{-0.156} & \underset{\pm 0.020}{-0.158} & 0 & 0 & 0 \\ & \underset{\pm 0.039}{0.483} & \text{N/A} & 0 & 0 & 0 \\ & & \underset{\pm 0.018}{0.517} & 0 & 0 & 0 \\ & & & \underset{\pm 0.073}{1.589} & 0 & 0 \\ & \text{Sym.} & & & \underset{\pm 0.109}{1.534} & 0 \\ & & & & & \underset{\pm 0.148}{1.891} \end{bmatrix}$$

Compliance matrix S in GPa^{-1}
for solid 90° configuration

$$\begin{bmatrix} \underset{\pm 0.036}{0.476} & \underset{\pm 0.025}{-0.156} & \underset{\pm 0.043}{-0.196} & 0 & 0 & 0 \\ & \underset{\pm 0.017}{0.473} & \underset{\pm 0.015}{-0.167} & 0 & 0 & 0 \\ & & \underset{\pm 0.038}{0.532} & 0 & 0 & 0 \\ & & & \underset{\pm 0.136}{1.768} & 0 & 0 \\ & \text{Sym.} & & & \underset{\pm 0.203}{1.549} & 0 \\ & & & & & \underset{\pm 0.251}{1.816} \end{bmatrix}$$

Compliance matrix S in GPa^{-1}
for solid ±45° configuration

$$\begin{bmatrix} \underset{\pm 0.025}{0.478} & \underset{\pm 0.009}{-0.164} & \underset{\pm 0.017}{-0.175} & 0 & 0 & 0 \\ & \underset{\pm 0.043}{0.465} & \text{N/A} & 0 & 0 & 0 \\ & & \underset{\pm 0.013}{0.470} & 0 & 0 & 0 \\ & & & \underset{\pm 0.160}{1.342} & 0 & 0 \\ & \text{Sym.} & & & \underset{\pm 0.169}{1.356} & 0 \\ & & & & & \underset{\pm 0.203}{1.587} \end{bmatrix}$$

Compliance matrix S in GPa^{-1}
for sparse 0.25 mm configuration

$$\begin{bmatrix} \underset{\pm 0.050}{1.023} & \underset{\pm 0.033}{-0.446} & \underset{\pm 0.048}{-0.305} & 0 & 0 & 0 \\ & \underset{\pm 0.050}{1.023} & \underset{\pm 0.039}{-0.174} & 0 & 0 & 0 \\ & & \underset{\pm 0.061}{0.621} & 0 & 0 & 0 \\ & & & \underset{\pm 0.240}{2.521} & 0 & 0 \\ & \text{Sym.} & & & \underset{\pm 0.214}{2.479} & 0 \\ & & & & & \underset{\pm 0.089}{2.212} \end{bmatrix}$$

Compliance matrix S in GPa^{-1}
for sparse 0.50 mm configuration

$$\begin{bmatrix} \underset{\pm 0.127}{1.032} & \underset{\pm 0.113}{-0.582} & \underset{\pm 0.102}{-0.401} & 0 & 0 & 0 \\ & \underset{\pm 0.127}{1.032} & \underset{\pm 0.020}{-0.208} & 0 & 0 & 0 \\ & & \underset{\pm 0.037}{0.753} & 0 & 0 & 0 \\ & & & \underset{\pm 0.369}{3.432} & 0 & 0 \\ & \text{Sym.} & & & \underset{\pm 0.147}{3.522} & 0 \\ & & & & & \underset{\pm 0.108}{3.224} \end{bmatrix}$$

Compliance matrix S in GPa^{-1}
for sparse 0.75 mm configuration

$$\begin{bmatrix} \underset{\pm 0.242}{1.149} & \underset{\pm 0.147}{-0.581} & \underset{\pm 0.090}{-0.418} & 0 & 0 & 0 \\ & \underset{\pm 0.242}{1.149} & \underset{\pm 0.074}{-0.228} & 0 & 0 & 0 \\ & & \underset{\pm 0.065}{0.947} & 0 & 0 & 0 \\ & & & \underset{\pm 0.299}{3.845} & 0 & 0 \\ & \text{Sym.} & & & \underset{\pm 0.636}{3.764} & 0 \\ & & & & & \text{N/A} \end{bmatrix}$$

Fig. 12. Compliance matrices describing the orthotropic elastic behavior of PEI Ultem processed by FFF in solid 0°, 90°, and ±45° and sparse 0.25 mm, 0.50 mm, and 0.75 mm configurations.

$S_{33} < S_{11}$ in all settings. This effect is because the air gap separation involves eliminating the intra-layer filament unions, but not the inter-layer cohesion. A similar effect is found in component S_{66}. In the solid ±45° samples, the intra-layer unions are stiffer than inter-layer ones, so $S_{66} > S_{55} \approx S_{44}$. In contrast, in all sparse configurations $S_{66} < S_{55} \approx S_{44}$ as the intra-layer filament unions are removed. Finally, a different trend from the solid ±45° configuration is observed when analyzing extension-extension coupling coefficients, as $S_{12} < S_{13} < S_{23}$ in all sparse cases.

4. Conclusions

The reported results are conclusive experimental evidence of the role that the infill parameters have on the mechanical performance and weight reduction of PEI Ultem processed by FFF under multiple load conditions.

Overall, the mechanical behavior of the printed parts depends on the material, and particularly on the FFF manufacturing parameters. The above analysis shows that the orientation and the infill settings have a direct impact on the stiffness, the resilience, the maximum stress, and the type of failure of the processed parts. Consequently, the appropriate control of these design parameters would allow manufacturing final parts with optimal performance.

The obtained results indicate that both the intra-layer and the inter-layer bonds play a significant role in the behavior of the FFF samples. In this sense, the use of the thermal chamber reduces the temperature gradient between the deposited filament and the last layer built. This fact strengthens the unions, improves mechanical performance, and decreases the degree of orthotropy. Furthermore, the results obtained confirm that the stiffness on the direction of the extruded filament is higher than the one of the intra-layer unions between contiguous filaments. However, the rigidity of the inter-layer cohesion of adjacent layers is the lowest.

The use of the air gap in the design of the infill leads to a meaningful reduction of the manufacturing costs associated with the material and production time. The results of the mechanical tests that were conducted prove that the sparse infill has a quantifiable impact on the specific mechanical properties. The specific values obtained by normalizing the test results by the mass of every sample are comparable to those achieved with the solid configurations or even superiors, particularly in the strain range.

The calculated compliance matrices verify the inherent orthotropy of FFF technology. Results also ascertain the effect of the manufacturing parameters on the elastic behavior of the PEI Ultem printed parts. These matrices will be valuable for the validation of forthcoming numerical models addressing different infill configurations. The matrices analysis also enabled to determine a correlation between the FFF settings and the mechanical performance of the intra-layer and inter-layer unions.

Nevertheless, the development of FFF technology still has some open fronts. The behavior of the intra-layer unions depends to a large extent on the fact that the infill filaments are deposited as parallel as possible. Furthermore, special attention must be paid on the placement of the contour seam, as it can behave as a dramatic stress concentrator. All these facts can have a detrimental effect on the mechanical performance of the manufactured parts, thus being a challenge for FFF technology that should be further addressed.

Finally, this investigation contributes to the development of novel design-for-manufacturing strategies to obtain functional structural elements. This fact provides FFF with an outstanding competitive advantage in comparison to other AM technologies.

CRediT authorship contribution statement

Albert Forés-Garriga: Methodology, Validation, Investigation, Writing - original draft. **Marco A. Pérez:** Methodology, Conceptualization, Investigation, Writing - review & editing, Formal analysis, Funding acquisition. **Giovanni Gómez-Gras:** Methodology, Conceptualization, Investigation, Formal analysis. **Guillermo Reyes-Pozo:** Conceptualization, Formal analysis, Funding acquisition.

Declaration of competing interest

The authors declare that they have no known competing financial interests or personal relationships that could have appeared to influence the work reported in this paper.

Acknowledgments

This work has been supported by the Ministry of Science, Innovation and Universities through the project New Developments in Lightweight Composite Sandwich Panels with 3D Printed Cores (3DPC) - RTI2018-099754-A-I00; and by the RIS3CAT Llavor 3D Community co-financed by the Generalitat de Catalunya (ACCIÓ) through the project TRANSPORT COMRDI16-1-0010 - (2017-2020). The authors are very grateful to Ariadna Chueca de Bruijn for the constructive suggestions and for the assistance in conducting the experiments.

Data availability

The raw data required to reproduce these findings are available to download from Mendeley Data Repository: https://data.mendeley.com/datasets/xw37dn4549/draft?a=a54c51f6-d32f-4e4e-a3fb-1067f98a68d0.

References

[1] U.M. Dilberoglu, B. Gharehpapagh, U. Yaman, M. Dolen, The role of additive manufacturing in the era of Industry 4.0, Procedia Manuf 11 (2017) 545–554.

[2] K.S. Prakash, T. Nancharaih, V.V.S. Rao, Additive manufacturing techniques in manufacturing - an overview, Mater. Today 5 (2018) 3873–3882.

[3] A.J.J. Sheoran, H. Kumar, Fused deposition modeling process parameters optimization and effect on mechanical properties and part quality: review and reflection on present research, Mater. Today 21 (Part 3) (2020) 1659–1672, https://doi.org/10.1016/j.matpr.2019.11.296.

[4] B.A. Aloyaydi, S. Sivasankaran, H.R. Ammar, Influence of infill density on microstructure and flexural behavior of 3D printed PLA thermoplastic parts processed by fusion deposition modeling, AIMS Mater. Sci. 6 (2019) 1033–1048.

[5] J.R.C. Dizon, A.H. Espera Jr., Q. Chen, R.C. Advincula, Mechanical characterization of 3D-printed polymers, Addit. Manuf. 20 (2018) 44–67.

[6] D. Popescu, A. Zapciu, C. Amza, F. Baciu, R. Marinescu, FDM process parameters influence over the mechanical properties of polymer specimens: a review, Polym. Test. 69 (2018) 157–166.

[7] C. Gabor, M.A. Alin, D. Magli, T. Bedo, S.I. Munteanu, D. Munteanu, The optimization of the production procedure in relation to the mechanical properties of additively manufactured parts, Mater. Today 19 (2019) 1008–1013.

[8] T.D. McLouth, J.V. Severino, P.M. Adams, D.N. Patel, R.J. Zaldivar, The impact of print orientation and raster pattern on fracture toughness in additively manufactured ABS, Addit. Manuf. 18 (2017) 103–109.

[9] A.K. Sood, R.K. Ohdar, S.S. Mahapatra, Parametric appraisal of mechanical property of fused deposition modelling processed parts, Mater. Design 31 (2010) 287–295.

[10] C.W. Ziemian, R.D. Ziemian, Residual strength of additive manufactured ABS parts subjected to fatigue loading, Int. J. Fatigue 134 (2020) 105455, https://doi.org/10.1016/j.ijfatigue.2019.105455.

[11] S.-H. Ahn, M. Montero, D. Odell, S. Roundy, P.K. Wright, Anisotropic material properties of fused deposition modeling ABS, Rapid Prototyp. J. 8 (2002) 248–257.

[12] B. Wittbrodt, J.M. Pearce, The effects of PLA color on material properties of 3-D printed components, Addit. Manuf. 8 (2015) 110–116.

[13] C.-Y. Lee, C.-Y. Liu, The influence of forced-air cooling on a 3D printed part manufactured by fused filament fabrication, Addit. Manuf. 25 (2019) 196–203.

[14] J.M. Chacón, M.A. Caminero, E. García-Plaza, P.J. Núñez, Additive manufacturing of PLA structures using fused deposition modelling: effect of process parameters on mechanical properties and their optimal selection, Mater. Design 124 (2017) 143–157.

[15] G. Gómez-Gras, R. Jerez-Mesa, J.A. Travieso-Rodriguez, J. Lluma-Fuentes, Fatigue performance of fused filament fabrication PLA specimens, Mater. Design 140 (2018) 278–285.

[16] W.C. Smith, R.W. Dean, Structural characteristics of fused deposition modeling polycarbonate material, Polym. Test. 32 (2013) 1306–1312.

[17] M. Domingo-Espin, J.M. Puigoriol-Forcada, A.-A. Garcia-Granada, J. Llumà, S. Borros, G. Reyes, Mechanical property characterization and simulation of fused deposition modeling polycarbonate parts, Mater. Design 83 (2015) 670–677.

[18] I. Sedighi, M.R. Ayatollahi, B. Bahrami, M.A. Pérez, A.-A. Garcia-Granada, Mechanical behavior of an additively manufactured polycarbonate specimen: tensile, flexural and mode I fracture properties, Rapid Prototyp. J. 26 (2) (2019) 267–277, https://doi.org/10.1108/RPJ-03-2019-0055.

[19] B. Bahrami, M.R. Ayatollahi, I. Sedighi, M.A. Pérez, A.A. Garcia-Granada, The effect of in-plane layer orientation on mixed-mode I-II fracture behavior of 3D-printed polycarbonate specimens, Eng. Fract. Mech. 231 (2020) 107018.

[20] A.G. Salazar-Martín, M.A. Pérez, A.-A. García-Granada, G. Reyes, J.M. Puigoriol-Forcada, A study of creep in polycarbonate fused deposition Modelling parts, Mater. Design 141 (2018) 414–425.

[21] J.M. Puigoriol-Forcada, A. Alsina, A.G. Salazar-Martín, G. Gómez-Gras, M.A. Pérez, Flexural fatigue properties of polycarbonate fused-deposition modelling specimens, Mater. Design 155 (2018) 414–421.

[22] Stratasys, ULTEM™ 9085 Resin FDM: Thermoplastic Filament. Fit for High-Performance Applications, Technical Report 2019.

[23] Stratasys, Stratasys Materials Testing Procedure, Technical Report 2019.

[24] Stratasys, SDS ULTEM 9085 Natural Model Material, Technical Report 2017.

[25] L. Gasman, Additive aerospace considered as a business, in: F. Froes, R. Boyer (Eds.), Additive Manufacturing for the Aerospace Industry 2019, pp. 327–340.

[26] A. Ceruti, P. Marzocca, A. Liverani, C. Bil, Maintenance in aeronautics in an Industry 4.0 context: the role of augmented reality and additive manufacturing, J. Comput. Des. Eng. 6 (2019) 516–526.

[27] R.J. Zaldivar, D.B. Witkin, T. McLouth, D.N. Patel, K. Schmitt, J.P. Nokes, Influence of processing and orientation print effects on the mechanical and thermal behavior of 3D-printed ULTEM 9085 material, Addit. Manuf. 13 (2017) 71–80.

[28] A. Bagsik, V. Schöppner, Mechanical properties of fused deposition modeling Pards with Ultem* 9085, in: ANTEC 2011 Plastics, Boston.

[29] A. Bagsik, V. Schöppner, E. Klemp, FDM part quality manufactured with Ultem*9085, International Conference Polymeric Materials, 2010 , (Halle, Saale).

[30] A.W. Gebisa, H.G. Lemu, Influence of 3D printing FDM process parameters on tensile property of ULTEM 9085, Procedia Manuf 30 (2019) 331–338.

[31] K.P. Motaparti, Effect of Build Parameters on Mechanical Properties of Ultem 9085 Parts by Fused Deposition Modeling, Ph.D. thesis Missouri University of Science and Technology, 2016.

[32] K.I. Byberg, A.W. Gebisa, H.G. Lemu, Mechanical properties of ULTEM 9085 material processed by fused geposition modeling, Polym. Test. 72 (2018) 335–347.

[33] A.W. Gebisa, H.G. Lemu, Investigating effects of fused-deposition modeling (FDM) processing parameters on flexural properties of ULTEM 9085 using designed experiment, Materials 11 (2018) 1–23.

[34] S.H. Fard, S.M. Hashemi, On the strain-life fatigue parameters of additive manufactured plastic materials through used filament fabrication process, Addit. Manuf. 32 (2020).

[35] R.J. Zaldivar, T.D. Mclouth, G.L. Ferrelli, D.N. Patel, A.R. Hopkins, D. Witkin, Effect of initial filament moisture content on the microstructure and mechanical performance of ULTEM 9085 3D printed parts, Addit. Manuf. 24 (2018) 457–466.

[36] D.A. Roberson, A.R. Torrado Perez, C.M. Shemelya, A. Rivera, E. MacDonald, R.B. Wicker, Comparison of stress concentrator fabrication for 3D printed polymeric Izod impact test specimens, Addit. Manuf. 7 (2015) 1–11.

[37] A. Chueca de Bruijn, G. Gómez-Gras, M.A. Pérez, Mechanical study on the impact of an effective solvent support-removal methodology for FDM Ultem 9085 parts, Polym. Test. 85 (2020) 106433.

[38] ASTM D638-14, Standard Test Method for Tensile Properties of Plastics, ASTM International, West Conshohocken, PA, 2014.

[39] ASTM D790-17, Standard Test Methods for Flexural Properties of Unreinforced and Reinforced Plastics and Electrical Insulating Materials, ASTM International, West Conshohocken, PA, 2017.

[40] ASTM D5379 / D5379M-19, Standard Test Method for Shear Properties of Composite Materials by the V-Notched Beam Method, ASTM International, West Conshohocken, PA, 2019.

[41] T. Yao, J. Ye, Z. Deng, K. Zhang, Y. Ma, H. Ouyang, Tensile failure strength and separation angle of FDM 3D printing PLA material: experimental and theoretical analyses, Compos. B. Eng. 188 (2020).

[42] Y. Zhao, Y. Chen, Y. Zhou, Novel mechanical models of tensile strength and elastic property of FDM AM PLA materials: experimental and theoretical analyses, Mater. Design 181 (2019) 108089.